IET Radar, Sonar & Navigation

WILEY

The Institution of Engineering and Technology

ORIGINAL RESEARCH OPEN ACCESS

Drone Detection With a LTE450-Based Passive Radar

Bruno Demissie | Christian Steffes

Department Sensor Data & Information Fusion, Fraunhofer, FKIE, Wachtberg, Germany

Correspondence: Bruno Demissie (bruno.demissie@fkie.fraunhofer.de)

Received: 2 August 2025 | **Revised:** 12 October 2025 | **Accepted:** 29 October 2025

Handling Editor: Stephane Meric

Keywords: array signal processing | drone detection | long term evolution | passive radar

ABSTRACT

Passive reconnaissance solutions receive increased interest as unjammable fibre-optic drones represent a large number of UAVs in recent military conflicts. In order to equip critical infrastructure with an early warning system against drone attacks, it seems obvious to use the local communication infrastructure as illuminator for a passive radar. In Germany and other European countries, a blackout resistant LTE network in the 450 MHz band for critical infrastructure sites is currently rolled outed or already planned. In this contribution, we provide a proof of concept and present experimental results with a LTE450-based single- and multichannel passive radar for drone detection. To ease the signal processing while achieving a clearer ambiguity-function, only the reference elements contained in the OFDM symbols are used. For removing the dominant direct path contribution from the illuminator, an ad hoc approach is used which exploits the space-time structure of the received OFDM reference elements.

1 | Introduction

Apart from the paramount role of drones in the war in Ukraine, incidents close to airports and critical infrastructure in various European countries have shown the overall importance of being able to detect and track Unmanned Arial Vehicles (UAVs).

While most existing reconnaissance approaches rely on detecting active drones via their data links or communication protocols, passive drones such as unjammable fibre-optic drones or drones, following a pre-programmed flight path which do not emit signals, are particularly challenging. Common techniques achieving passive drone detection and tracking mainly adopt costly sensors such as radars, lidars or high-resolution cameras. An alternative much cheaper sensor is a passive radar system, as no transmitter is required and spectrum licence fees do not incur.

Passive radar, also known as passive coherent location (PCL) or passive covert radar (PCR), is a concept in which illuminators of opportunity are devoted to detect targets and estimate their positions and Doppler velocities. The advantage over active radar systems lies in reduced costs, the ability to operate covertly and hence being insusceptible against anti-radiation missiles or electronic countermeasures. Meanwhile, all kinds of available signals, such as analogue as well as digital audio or video broadcast [1–3], cellular phone networks [4], satellite signals [5] or wireless local areas networks [6, 7] have been investigated for passive radar purposes. The recent interest in using digital waveforms as illuminators of opportunity is by part due to the fact that they are exactly specified in technical norms which allows to reconstruct a multipath-free reference signal.

Due to the increasing thread posed by UAVs, numerous research and experiments for the detection of UAVs using passive radar have been reported in the literature. In particular, results obtained with illuminators in the neighbouring frequency bands of LTE450, that is, the frequency band directly above from 470 MHz up to 858 MHz used for DVB-T and Digital Terrestrial

Abbreviations: LTE, Long Term Evolution; OFDM, Orthogonal Frequency-Division Multiplexing; UAV, Unmanned Arial Vehicle.

Multimedia Broadcast (DTMB) and the lower frequency band from 174 MHz to 230 MHz used for DAB are of notable interest.

In [8], the successful detection of a DJI UAV (diameter ≈50 cm) up to a distance of 3 km was presented using an 8-channel PCL system. Additionally, the modulation caused by the rotor blades was used to discriminate UAVs from birds or other vehicles. In [9], a DJI Phantom 4 (35 cm; 1380 g) could be detected using two DTMB emitters (685 and 738 MHz, 7.5 km distance to PCL system) up to a distance of 2.25 km. For two SOTIKOL UAVs (diameter 0.5 and 1 m), a detection could be shown using DVB-T (770 MHz, 20 kW, 30 km distance to PCL system) in approximately 1 km distance. The detection of four UAVs was investigated in [10] using a DVB-T2 emitter (660 MHz, 49.2 km distance to PCL system). The four UAVs of type DJI Phantom 3 (length 40 cm), DJI F450 (length 45 cm), Geoscan 401 (length 150 cm) and a fixed wing model aircraft (rigid foam, wing spread 190 cm) were clearly detectable in Range-Doppler diagrams at distances between 750 and 900 m. A classification by considering the different Doppler signatures of the rotor speeds was possible (except for the smallest UAV with plastic blades). In [11], the PCL System AULOS using DVB-T (570 MHz, 50 kW, 22.5 km distance to PCL system) was used to detect a DJI Phantom 4 Pro and a DJI Mavic Pro. Both drones were detected and localised up to a bistatic distance of ≈5 km. Recently [12, 13], even a very small UAV of type PARROT AR.Drone 2.0 (length 15 cm) could be detected in a bistatic distance of 250 m (no coverage measurements were performed but even more seems possible) using DVB-T (562/594/634 MHz, 100 kW, 45 km distance to PCL system). The detection of a flying wing UAV Skywalker X-8 (wing span 2.1 m) using DAB illumination was shown by Schüpbach et al. [14]. A two channel PCL system was used and the highest detection rate of 36% was achieved using a DAB+ emitter (188.9 MHz, 5 kW, 12 km distance to PCL system) for distances of up to 1.2 km. Recently, Welschen et al. [15] presented results using a five channel system. Two hexacopter of type DJI S900 (diameter 90 cm) and DJI F550 (diameter 55 cm) were clearly detectable up to a distance of 2.6 km and 750 m using several DAB emitters (227.36 MHz). In [16], we gave an overview of the use cases of mobile communication based PCL and presented experimental results for UAV detection and tracking using GSM/LTE PCL and the fusion with camera sensors. Although all of these results obtained with DVB-T/DAB are very promising, there are two drawbacks: The radio coverage is known to be quite poor in valleys. Furthermore, in some regions, DVB-T uses vertical polarization, thus leading to much weaker reflections of the carbon fibre rotor blades of multicopters.

In many European countries, critical infrastructure will be equipped with an independent blackout-proof wireless communication network named LTE450 operating at a centre frequency of 467.37 MHz and a bandwidth of up to almost 5 MHz. This frequency band with wavelength of about 64 cm seems suitable for drone detection [17] as it lies in the optimal frequency region concerning the received power reflected off the target and which is influenced by two opposing trends: on the one hand, the path loss increases with rising frequency, whereas, on the other hand, the radar cross section decreases rapidly in the Rayleigh scattering region where the wavelength is longer than the size of the target. This is illustrated in Figure 1

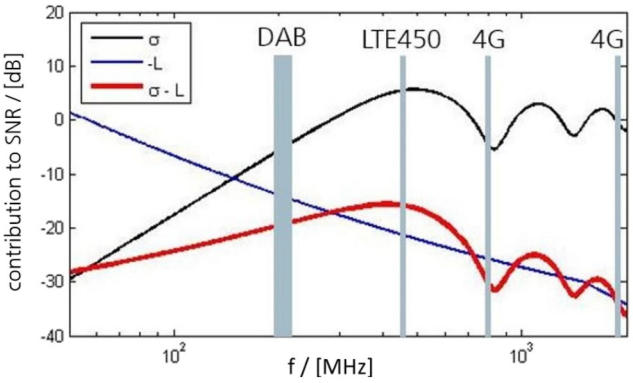

FIGURE 1 | Contributions to the SNR: RCS σ of a sphere, negative of propagation path loss $-L$ and sum of both as a function of frequency.

which shows the (negative of the) path loss according to the COST231-Hata propagation model [18] and the Radar Cross Section (RCS) of a sphere [19] with radius $R = 10$ cm, serving as rough model for a small UAV as a function of the carrier frequency. The later decreases with the fourth power of the frequency in the Rayleigh scattering regime and has a local maximum close to the LTE450 frequency band before it starts to oscillate in the optical region. According to the radar equation, the sum of both terms contributes to the SNR at the radar.

In our previous work [17], we analysed and discussed the requirements for a successful operational use of an LTE450-based PCL system based on a purely theoretical analysis and interpolation of experimental results with other PCL illuminators in adjacent frequency bands below and above LTE450. This contribution provides a proof of concept via experimental results obtained with a single channel and a multichannel receiver. For a single receiving channel we present range measurements with a medium-sized UAV which have already been published in a submission to a radar conference in [20]. The results for a multichannel receiver contain statistical performance evaluations of target parameters as well as probabilities of target detection. Furthermore, we describe the signal processing steps for an efficient range-Doppler processing in which only the reference elements of the LTE downlink are exploited. Although there is a certain loss in SNR, this approach offers many advantages: the demodulation of the illuminating signal can be omitted as it is exactly given in ETSI specifications. Inverse filtering may be applied without loss of SNR. Efficient approaches for direct path cancellation may be applied—whereby two novel ad hoc approaches are presented in this contribution.

2 | Signal Processing

2.1 | Data Model for Received Signal

The waveform of a LTE downlink signal is given in the ETSI Technical Specification TS 36.211 [21]. Here, we consider only the reference elements (RE). The value p of the so-called antenna port determines which OFDM-Symbols in a time slot (TS) contain REs. (One TS consists of seven OFDM symbols.) For $p = 1, 2$, the first and the fifth OFDM symbols contain REs on

each sixth subcarrier with offset $k_0 = 1, .., 6$ in the first symbol and with offset $\mathrm{mod}(k_0 + 3, 6)$ in the fifth symbol. The offset is determined by the Cell ID. For $p = 3, 4$, only the second OFDM-symbol in each TS contains reference elements. If we define the index set of all subcarriers in the l-th OFDM symbol containing reference elements $\mathbb{K}_{k_0(l)} = \{-N_{\mathrm{RB}}^{\mathrm{DL}} N_{\mathrm{sc}}^{\mathrm{RB}}/2 + k_0(l) - 1, ..., -7 + k_0(l), k_0(l), ..., N_{\mathrm{RB}}^{\mathrm{DL}} N_{\mathrm{sc}}^{\mathrm{RB}}/2 + k_0(l) - 6\}$, where $N_{\mathrm{RB}}^{\mathrm{DL}} = 15$ for a bandwidth of 3 MHz and $N_{\mathrm{sc}}^{\mathrm{RB}} = 12$, the waveform in the l-th OFDM symbol is given by the following equation:

$$s_l(t) = \sum_{k \in \mathbb{K}_{k_0(l)}} a_{k,l} e^{j2\pi k \triangle f t}, \tag{1}$$

where $a_{k,l}$ are Quadrature Phase Shift Keying (QPSK) symbols. The subcarrier spacing is $\triangle f = 15$ kHz and the time $t \in [0, NT_S]$ is assumed to be in the active part of the OFDM symbol, that is, discarding the cyclic prefix as in the usual demodulation step. The elementary time unit is $T_S = 1/(15000 \cdot N)$ seconds with $N = 2048$ the FFT length of the OFDM symbol.

We assume that the eNodeB transmits L time slots with carrier frequency f_c, and the bandwidth of each pulse satisfies $W \ll f_c$. (In radar terminology we may consider one TS as one pulse.) The transmitted pulses have nonzero power spectra only for positive frequencies allowing to write the analytic signal in the form as follows:

$$s(t) = \sum_{l=1}^{L} s_l(t - (l-1)T_{\mathrm{P}}) e^{j2\pi f_c t}, \tag{2}$$

where $T_{\mathrm{P}} = 15360 T_S$ is the time-lag of consecutive pulses. (This holds for antenna ports $p = 3, 4$. For antenna ports $p = 1, 2$, there are two OFDM-symbols per TS, of course. However, for the sake of simplicity we consider only the case of one OFDM symbol per TS, in the following.) The coherent integration time (CIT) is $T_{\mathrm{CIT}} = LT_{\mathrm{P}}$. It should be selected to span the interval over which the received signal is phase coherent.

The transmitted signal is reflected at P targets and reaches the receiver with delays $\tau_p(t), p \in \mathbb{N}_P{}^+$ (The set of non-negative integers is denoted $\mathbb{N}_P{}^+ = \{1, ..., P\}$). When the transmitter, targets or receiver exhibit relative motion, the delays depend themselves on the actual time causing contractions/dilations of time. Formally, the received signal can be described using a time-dependent channel transfer function as follows:

$$h(t, \tau) = \sum_{p=1}^{P} \hat{\gamma}_p(t) \delta\big(\tau - \tau_p(t)\big), \tag{3}$$

where $\hat{\gamma}_p$ is the attenuation of the p-th propagation path, which is, in principle, time-varying, due to a dependency of the bistatic radar cross section (RCS) on the relative orientation of the target or due to other reasons such as propagation effects. Dirac's δ-distribution is denoted $\delta(\cdot)$. Assuming a non-relativistic and linear model, $\tau_p(t) = \tau_p - \nu_p t/f_c$, for the time-dependent delays over the observation interval, where ν_p is the Doppler shift of the p-th target, the received signal after frequency down-conversion reads as follows:

$$x(t) = e^{-j2\pi f_c t} \int_{-\infty}^{\infty} h(t, \tau) s(t - \tau) d\tau \tag{4}$$

$$= \sum_{p=1}^{P} \sum_{l=1}^{L} \gamma_p(t) s_l\big(t - (l-1)T_{\mathrm{P}} - \tau_p + \nu_p t/f_c t\big) e^{j2\pi\nu_p t}, \tag{5}$$

where we have absorbed the phase due to the delay in $\gamma_p = \hat{\gamma}_a e^{-j2\pi f_c \tau_p}$. The complex envelope $s(t)$ is slowly varying and can be approximated as $s_l\big(t - \tau_p + \nu_p t/f_c\big) \approx s_l\big(t - \tau_p\big)$ if the condition $WT_{\mathrm{CIT}}|\nu_p|/f_c \ll 1$ is fulfilled. Otherwise, for large bandwidth, for which the range cells are small, and for sufficiently high Doppler velocity, the target moves from one range cell to another during the observation interval, leading to range migration which is not considered here.

In the following, the received data model is discretised in time. We sample the received signal with a rate $F_{\mathrm{S}} = T_S^{-1}$ at sampling instants $t_{n,l} = nT_S + (l-1)T_{\mathrm{P}}, n \in \mathbb{N}_N{}^+, l \in \mathbb{N}_L{}^+$. In radar terminology, T_S corresponds to the fast time and T_{P} to the slow time.

In order to be able to arrive at a signal model that is a sum of P rank-one two-way components, we make the following assumptions:

A1 The phase due to the Doppler shift is piecewise constant during the duration T_{P} of a single pulse: $e^{j2\pi\nu_p t_{n,l}} \approx e^{j2\pi(l-1)T_{\mathrm{P}}}$.

A2 The path attenuation is constant during the CIT $\gamma_p\left(t_{n,l}\right) = \gamma_p e^{j2\pi T_{\mathrm{P}}}$.

A3 During the observation period the delay τ_p is constant.

Assumption *A1* leads to the restriction that the Doppler shift is smaller than half the pulse repetition frequency (PRF) $|\nu_p| < \frac{1}{2} \triangle f$ in order to achieve an unambiguous Doppler frequency. This corresponds to a Doppler velocity of $|v_{\mathrm{D}}| < 4800\ m/s$ which is certainly fulfilled for drones. The second assumption is fulfilled in realistic conditions as the pulse duration is a fraction of a millisecond. The fulfilment of assumptions *A3* depends on the particular scenario of the moving targets relative to the length of the observation period.

Inserting these approximations, the samples are then arranged in a matrix $\mathbf{X}$ with elements as follows:

$$\mathbf{X}_{n,l} = x\big(t_{n,l}\big) = \sum_{p=1}^{P} \gamma_p s_l\big(nT_S - \tau_p\big) e^{j2\pi\nu_p l T_{\mathrm{P}}}, \tag{6}$$

2.2 | Range-Doppler Processing

Range processing usually consists in cross-correlating the received signal with the reference signal. (More precisely, we are dealing with bistatic ranges due to illuminator-receiver constellation in passive radar. The bistatic range is related to the propagation delay via $r_p = c\tau_p$.) Here, this is carried out in Fourier space according to the convolution theorem as a length-N FFT of each OFDM symbol appears naturally within

the demodulation step, as mentioned earlier in [22]. Due to the orthogonality between the Fourier modes and the OFDM subcarriers, the received signal after applying a FFT to each column of $\mathbf{X}$ reads as follows:

$$\mathbf{S}_{k,l} = a_{k,l} \sum_{p=1}^{P} \gamma_p e^{-j2\pi k \triangle f \tau_p} e^{j2\pi \nu_p l T_{\mathrm{P}}}. \tag{7}$$

At this point, it is possible to select only those subcarriers which contain REs. In order to reduce the subsequent computing effort, a signal matrix of size $2N\mathrm{RB}^{\mathrm{DL}} \times L$ is constructed by concatenating only the REs. Dividing all elements in $\mathbf{S}$ by the symbols $a_{k,l}$, that is, multiplying with the complex-conjugates $a^*_{k,l}$ as they have unit magnitude, leads to a signal matrix in Fourier space,

$$\mathbf{Y}_{k,l} = \sum_{p=1}^{P} \gamma_p e^{-j2\pi k \triangle f \tau_p} e^{j2\pi \nu_p l T_{\mathrm{P}}}, \tag{8}$$

relieved of the particular values of the REs. This approach has been exposed in [23] and is known in a more general context as inverse filtering or mismatched filtering [24]. Executing a column-wise inverse FFT eventually achieves range processing. Following [22], Doppler processing is accomplished by means of an FFT along the rows of the latter matrix. The output of the mismatched/matched filter for range-Doppler processing is given by the matrix as follows:

$$\mathbf{Z}_{n,i} = \sum_{l=1}^{L} \sum_{k=1}^{K} \mathbf{Y}_{k,l} e^{-j2\pi(l-1)(i-1)/L} e^{j2\pi(k-1)(n-1)/K}, \tag{9}$$

where the index n labels the bistatic range cell and i labels the Doppler cell. In order to decide whether in the (n, i)-th bistatic range-Doppler cell a target is present or just noise, only those values $C(r_n, \nu_i) = |\mathbf{Z}_{n,i}|^2$ exceeding a threshold η will be counted as positive detections. The threshold is estimated from a set of bistatic range-Doppler cells in which presumably no target is present and is related to a predetermined probability of false alarm, see [19].

2.3 | Multichannel Signal Processing

Furthermore, we assume that the multi-path signal is received with an antenna array consisting of a set of M sensors. The response of the sensors which spatially sample the wave-field of the p-th multi-path component is contained in the steering vector $\mathbf{a}(\theta_p) \in \mathbb{C}^{M\times 1}$ depending on the direction-of-arrival θ_p. The multichannel received signal in Fourier space after elementwise multiplication is arranged in a three-way array as follows:

$$\mathcal{X}_{m,k,l} = \sum_{p=1}^{P} \gamma_p \mathbf{a}_m(\theta_p) e^{-j2\pi k \triangle f \tau_p} e^{j2\pi \nu_p l T_{\mathrm{P}}}. \tag{10}$$

After applying the range-Doppler processing steps as above to each of the M channels separately, a beamformer is applied to the first dimension of the three-way array in each range and Doppler cell.

2.4 | Direct Path Cancellation

In most passive radar systems the direct signal is suppressed by Least-Squares (LS) approaches or adaptive filters [25]. Another approach achieving quite often results superior to the above approaches due to the fact that an exact reference signal is not required is a delay-line canceller (DLC) [26] which is applicable to the REs as they repeat every twenty TS. Here, we pursue the following ad hoc approach: Introducing the diagonal matrix $\Gamma = \mathrm{diag}(\gamma_1, ..., \gamma_P)$ and matrices $\mathbf{B}_{k,p} = e^{-j2\pi k \triangle f \tau_p}$ and $\mathbf{C}_{l,p} = e^{-j2\pi \nu_p l T_{\mathrm{P}}}$, the above model for the received signal in Fourier space can be written as follows:

$$\mathbf{Y} = \mathbf{B}\Gamma\mathbf{C}^H. \tag{11}$$

This matrix decomposition comes very close to a singular value decomposition (SVD) as the matrices $\mathbf{B}$ and $\mathbf{C}$ are almost unitary matrices if the multi-path components are sufficiently separated in bistatic range and Doppler. For a CIT of one second, two multi-path components are already orthogonal in Doppler if they differ by more than 1 Hz. Concerning the orthogonality in bistatic range, two targets have to lie in two different bistatic range cells whose width is dictated by the bandwidth of the illuminator. The SVD of the received signal is given by the following equation:

$$\mathbf{Y} = \mathbf{U}\Sigma\mathbf{V}^H. \tag{12}$$

The direct signal presumably corresponds to the two-way rank-one component with the largest singular value σ_1 and singular vectors $\mathbf{u}_1, \mathbf{v}_1$. Subtracting this pair from the signal matrix should remove the direct path as follows:

$$\tilde{\mathbf{Y}} = \mathbf{Y} - \sigma_1 \mathbf{u}_1 \mathbf{v}_1^H. \tag{13}$$

This is, of course, just an approximation to a perfect direct path subtraction. In some situations where local scattering around the receiver exists, one may subtract one or few more singular vectors with large singular value.

Next, we turn to the multichannel signal model. Typical approaches for suppressing the direct signal in the spatial domain use adaptive beamformers. Here, we extend the above ad hoc approach to the three-way array. Defining the steering matrix as $\mathbf{A} = \mathbf{a}(\theta_1)\cdots\mathbf{a}(\theta_P)]$ the three-way array may be expressed as follows:

$$\mathcal{X}_{m,k,l} = \sum_{p=1}^{P} \Gamma_p \mathbf{A}_{m,p} \mathbf{B}_{k,p} \mathbf{C}_{l,p}. \tag{14}$$

This representation is known as PARAFAC decomposition [27]. It may be considered as a third-order generalisation of the matrix SVD and, in an analogous way, the trilinear rank-one component with the largest power presumably originates from the direct path.

The following example with a synthetically generated multi-path signal will illustrate this approach. In the simulations, there are six targets on a straight line, starting with one target having zero bistatic range. Furthermore, there is a seventh target with large bistatic range and zero Doppler. The scenario with the direct path at zero bistatic range and Doppler is shown in Figure 2. In order not to mask the targets, the direct path is

weakened in the latter figure. The same target with the direct path having full strength of 40 dB higher than each of the targets having equal power is shown in Figure 3.

Applying a delay-line-canceller leads to a satisfactory suppression of the direct path, see Figure 4. However, this comes with the drawback that the two targets at exactly zero bistatic range and zero Doppler are cancelled completely, as well. Furthermore, the two targets with Doppler 4 and 100 Hz close to a Doppler notch are weakened.

Subtracting the principal singular vector according to the SVD-based ad hoc method completely eliminates the direct path, see Figure 5. Only the two targets at exactly zero bistatic range and zero Doppler are cancelled, as well. This is due to the fact that for these targets either the left or the right singular vector is collinear to the one of the direct path. All other targets are not weakened. Finally, applying the ad hoc approach based on subtracting the dominant rank-one component of the PARAFAC decomposition leads to a perfect direct path cancellation where all targets are not suppressed at all, see Figure 6.

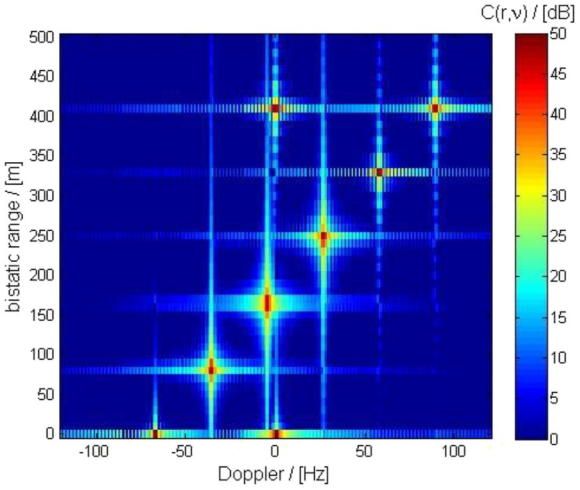

FIGURE 2 | Scenario with six targets placed equidistant on a diagonal and one target with zero Doppler at bistatic range $r = 400$ m. The direct path is weakened.

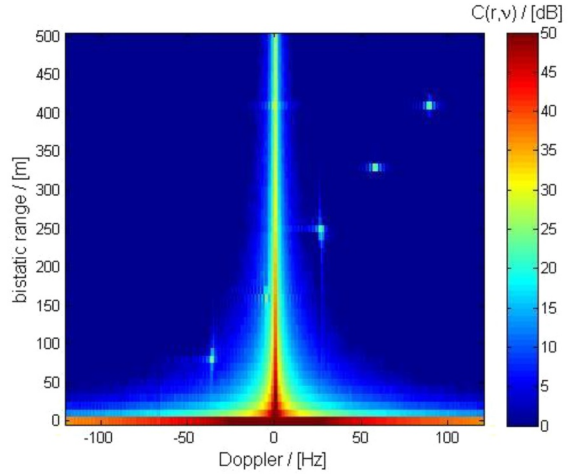

FIGURE 3 | Same scenario as in Figure 2 with the direct path having full strength and overshining some targets.

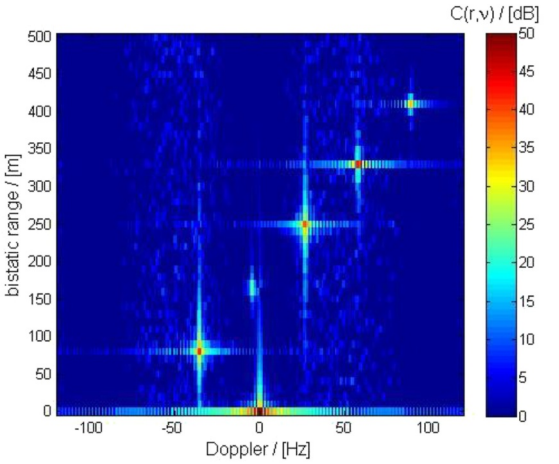

FIGURE 4 | Direct path cancellation via delay-line-canceller.

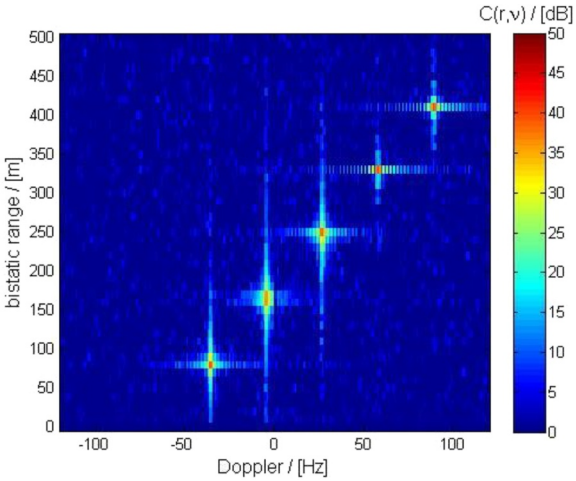

FIGURE 5 | Direct path cancellation via subtraction of dominant singular vectors.

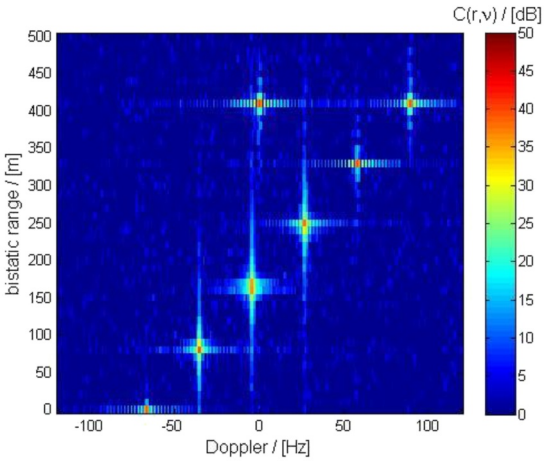

FIGURE 6 | Direct path cancellation via subtraction of dominant three-way rank-one component.

3 | Passive Radar System Description

Our experimental system is built up using commercial off-the-shelf components. For the work presented here, a simple setup using an Ettus USRP X310 equipped with TwinRX daughterboards and a workstation PC to control the USRP and to process the received data was chosen. The signals are digitized at a sample rate of 200/6 MHz (caused by the TwinRx master clock rate). Due to hardware restrictions of our experimental system, continuous data streaming is not possible. Therefore, we recorded each second scans of 26,666,640 samples per channel corresponding to a coherent integration time of $T = 0.8$ sec. Afterwards, the signal is resampled to the LTE sample rate of 30.72 MHz. In the single receiver setup, two different antenna types—a patch and a log per antenna with different polarisations—were used in order to study the influence of the polarization of the receiving antenna.

The multichannel passive radar uses a uniform linear antenna array consisting of four Yagi antennas orientated horizontally. A picture of the antenna array is shown in Figure 7. The horizontal polarization for the receiving antenna is chosen since our recent experiments [20] with a LTE450 eNodeB revealed a significant advantage over a vertically polarised antenna. This is mainly due to the carbon fibre rotor blades of drones reflecting the radiation from the illuminator. However, the design frequency of the array had to be set lower due to the structural shape of the antennas and the associated minimum distance between two array elements.

FIGURE 7 | View on the four-element antenna array on the roof of a building at the site of Fraunhofer FKIE.

4 | Experimental Results

A DJI Matrice M210 was chosen as target for our experiments. The UAV has as size of approx. 88 × 88 × 39 cm, weighing slightly less than 5 kg. A GPS logger was installed on the UAV and its data are used as ground truth in the evaluation step. For our first experiments with a single surveillance channel, the goal was to get as close as possible to a monostatic setup. Since the LTE450 network is currently being deployed in Germany, only a small number of base stations were in operational mode at the time. We chose a base station in the south west of Cologne, with the possibility to perform test flights over agricultural fields. The scenario including the positions of the base station and the experimental system as well as the trajectory of the UAV for two investigated trials are given in Figure 8. A picture of the experimental setup can be found in [20].

The goal was to find out the maximum range at which the drone can be detected with a single surveillance channel. The first trial served as a coarse exploration of the maximum range. For small bistatic ranges, it was possible to detect the drone safely, that is, with a probability of detection $P_D = 1$ for extremely small false alarm rates, compare the range-Doppler plot Figure 9 for a target at bistatic range $R \approx 500$ m in the cell-under-test (CUT) with centre given by the ground truth. In this figure, the box containing the reference cells for estimating the false alarm rate P_{fa} is indicated, as well. The position of the box was chosen in the best possible way neither to contain any of the target's range or Doppler side lobes nor any of the ambiguity artefacts of the direct signal. As the UAV flies away, the less pronounced is the peak of the reflection, see Figure 10 for a bistatic range of 2690 m. Finally, it becomes more and more unclear whether a peak originates from a target reflection or is just due to noise. This uncertainty can only be resolved using a statistical approach from detection theory. Under the null hypotheses, that is, when no target signal is present, one can require a certain probability of false alarm P_{fa} and estimate the decision threshold from the corresponding probability distribution.

In this light, the second trials have been evaluated systematically. The thresholds for decreasing false alarm rates $P_{\text{fa}} = 0.01, 0.001, 0.0001$ have been estimated from the reference cells of all available batches containing a sample size of $N_{\text{fa}} = 737704$ samples. In Figure 11, the maximum in the CUT and the thresholds for three false alarm rates are plotted along the path of the UAV as a function of the bistatic range. As

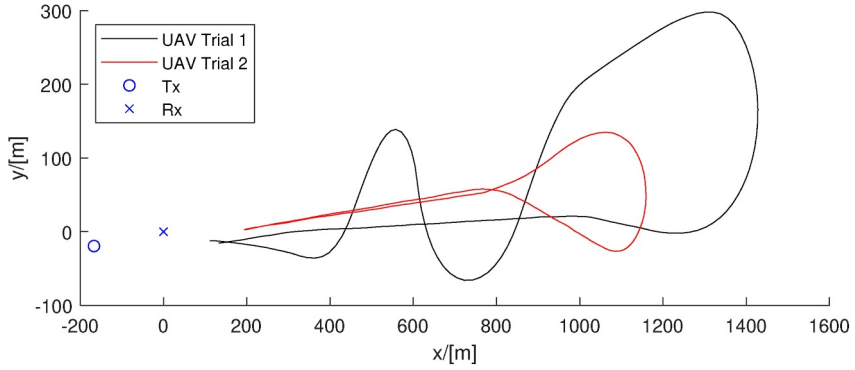

FIGURE 8 | Positions transmitter, single-channel receiver and flight path of UAV.

expected, the threshold increases with decreasing false alarm rate. As a consequence, given $P_{fa} = 0.0001$, the drone can be detected up to a bistatic range of about 1600 m.

The power in the CUT displays an oscillatory behaviour which depends strongly on the particular measurement position and reflectors in the surrounding thereof. This oscillatory pattern is typical for the interference of two propagation path, one direct path and one reflection. In order to make a more general statement about the maximum possible range, we consider only the maxima of the oscillatory curve. Theoretical considerations concerning the path loss as a function of the range predict a linearly decaying behaviour on a double logarithmic plot which is indeed confirmed in Figure 11 containing a linear fit through the peaks of the oscillations. This allows to define the maximal possible range as a function of the false alarm rate through the intersection of the corresponding threshold with the linear fit to the peaks of the power decay.

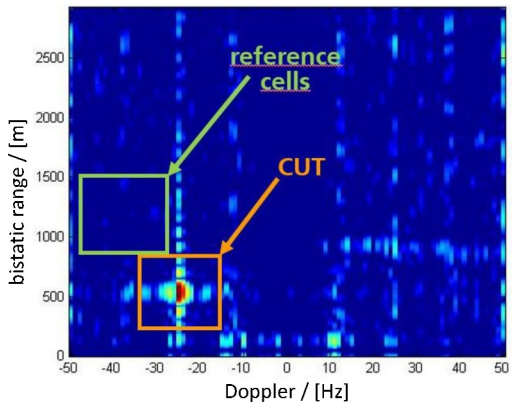

FIGURE 9 | Bistatic range/Doppler cells $|\mathbf{Z}_{n,i}|^2$ containing a target at bistatic range $r \approx 500$ m.

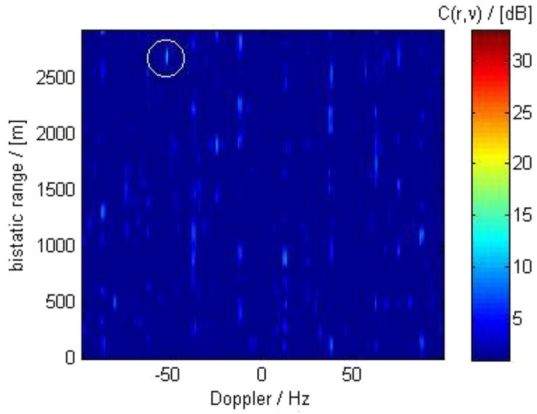

FIGURE 10 | Range-Doppler plot of a target at bistatic range $r \approx 2690$ m. The white circle indicates the ground truth.

The goal of the second experiment was to transfer the results of the single surveillance channel approach to a multichannel system. Since we use a uniform linear array, the measurement space is now three-dimensional with the azimuth in addition to range and Doppler. For the experiments with our multichannel PCL system, two different eNodeBs at about 10.8 km distant from the receiver (base station 1), and about 9.6 km far of the receiver (base station 2), were used as illuminators of opportunity. The drone flew 30 m above ground and made a loop in clockwise direction with a speed of about 10 m/sec.

In the following, we investigate two flights with the aforementioned drone and clockwise loops. The corresponding trajectories as well the positions of the receiver and the illuminators are depicted in Figure 12. The bistatic geometry for both base stations is quite similar. At the time of our experiments, however, only these two base stations in the proximity of the test site were on air, as the network is currently in the rollout phase.

The results for the two flight paths and eNodeBs are given in Figures 13–16. We chose a Doppler-time depiction of the four-dimensional data (range, Doppler, azimuth, time), where for each Doppler cell, the maximum of the corresponding range and azimuth values is given. The ground truth is plotted as a white dotted line.

As can be seen, the drone is detected during most of the flight path. The detection gap for flight path 1 approximately in the middle of the trajectory is probably due to the geometry of our experimental setup. For flight path 2, the detection using both base stations is nearly without gaps. The errors for all measurement dimensions as well as the probability of detection are given in Table 1. Range errors seem as expected, considering the

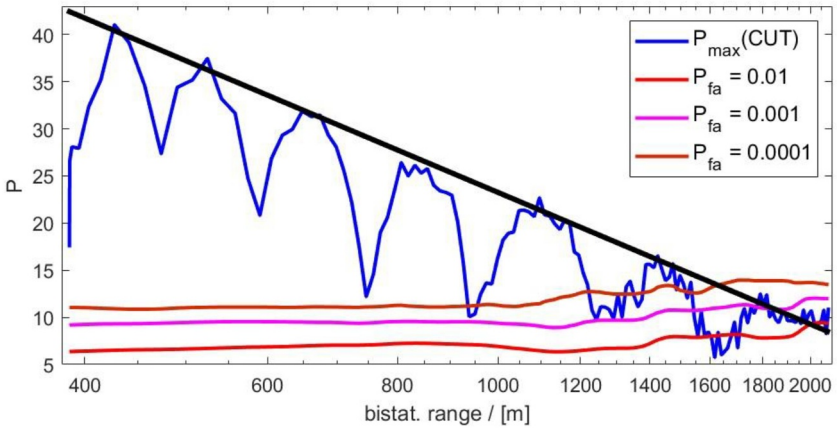

FIGURE 11 | Double-logarithmic plot of the maxima in the CUT versus bistatic range. A linear fit to the peak values is added.

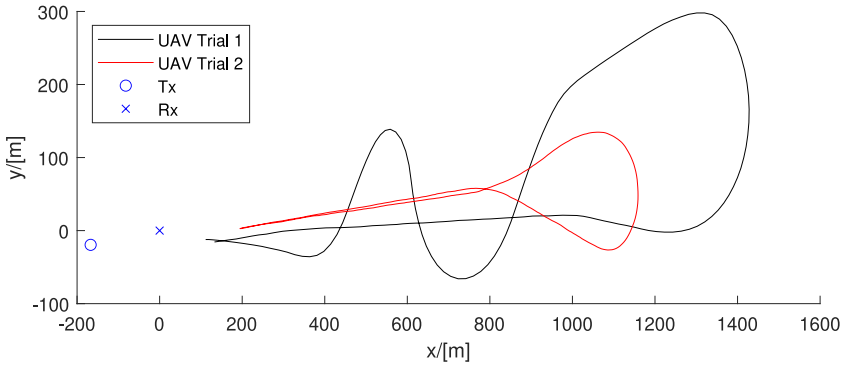

FIGURE 12 | Scenario including two LTE450 base station as illuminators and one multichannel receiver.

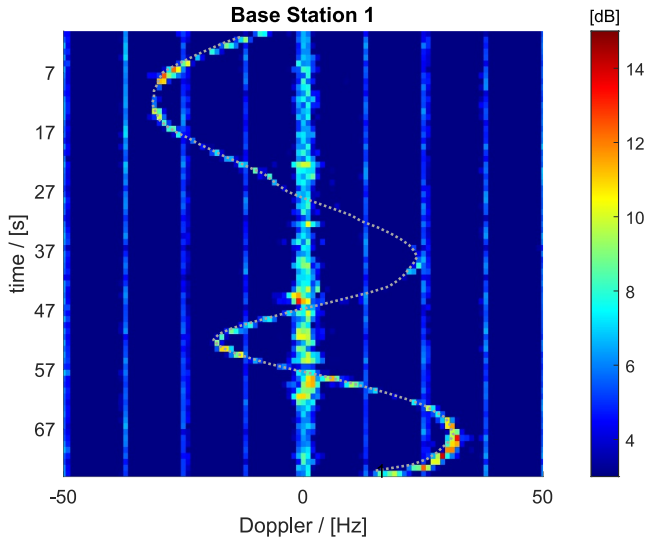

FIGURE 13 | Flight path 1: Doppler-time results for base station 1. Dotted grey line: ground truth derived from GPS data.

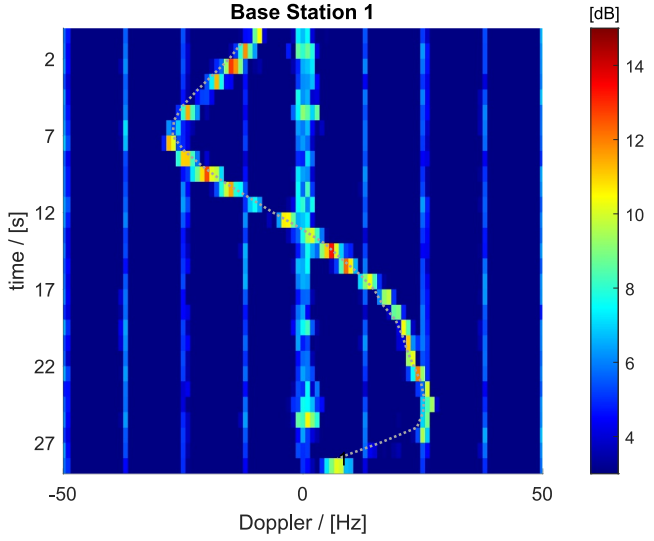

FIGURE 15 | Flight path 2: Doppler-time results for base station 1. Dotted grey line: ground truth derived from GPS data.

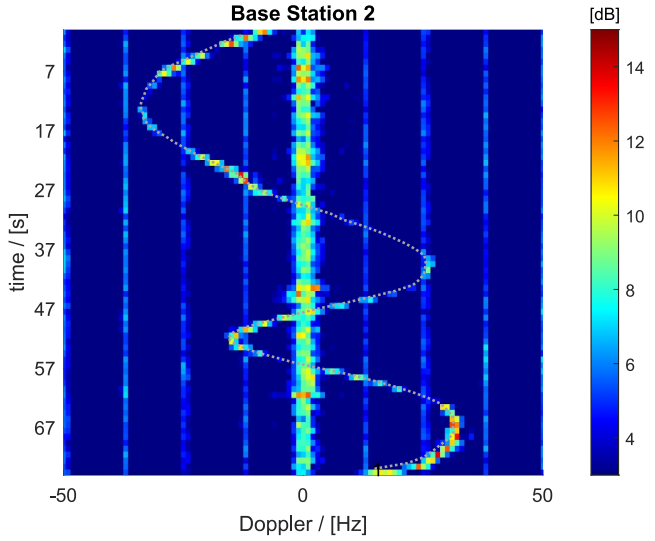

FIGURE 14 | Flight path 1: Doppler-time results for base station 2. Dotted grey line: ground truth derived from GPS data.

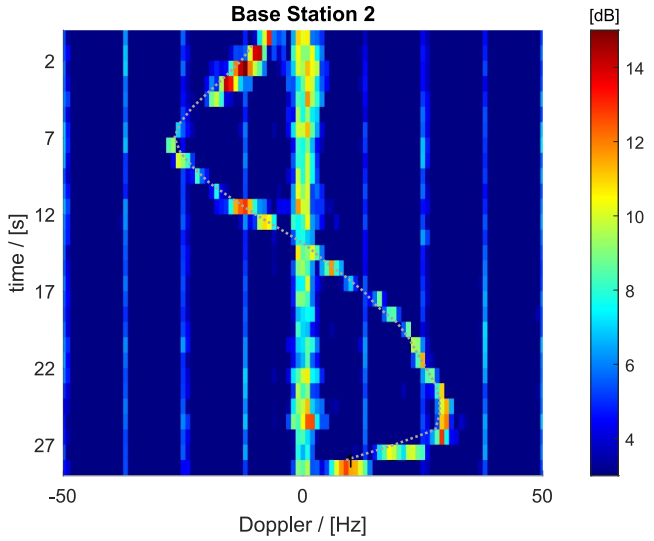

FIGURE 16 | Flight path 2: Doppler-time results for base station 2. Dotted grey line: ground truth derived from GPS data.

TABLE 1 | Measurement errors and probabilities of detection of multichannel experiments.

	Flight path 1		Flight path 2	
eNodeB	**Base station 1**	**Base station 2**	**Base station 1**	**Base station 2**
Range in [m]	0.93 ± 15.7	10.0 ± 13.7	7.82 ± 8.8	10.4 ± 9.1
Doppler in [Hz]	0.54 ± 0.8	0.45 ± 1.1	0.61 ± 1.7	0.32 ± 1.3
Azimuth in [deg]	2.8 ± 2.4	2.2 ± 3.7	2.6 ± 3.8	2.3 ± 3.7
$P_d(P_{fa} = 0.008)$	79.7	81.1	96.4	75.0

sampling frequency, the Doppler is estimated with high accuracy. The detection rate is quite high, the value for base station 2 at flight path 2 is probably due to the short experiment duration with only a few missed detections (compare Figures 15 and 16). For this evaluation, we declare a measurement to be a detection and calculate the measurement errors, if it is above a threshold and within a certain window of the true value in measurement space given by the ground truth.

5 | Conclusions

In the future, inexpensive small drone or loitering ammunition swarms could be used rather than expensive precision weapons such as cruise missiles, especially in attacks on highly decentralised energy systems. This scenario is particularly likely considering the ongoing decentralisation of the energy system as a result of the energy transition, as high-value targets such as large power plants are increasingly being replaced or complemented by decentralised energy resources such as wind or solar.

The defence against these threats therefore requires intrusion detection systems that can detect individual drones or swarms within a range of at least 1 km, regardless of the time of day or weather. Currently, the legal situation in Germany does not allow for the use of countermeasures by private organisations or operators of critical infrastructures. Therefore, the initial focus has been on detection to become aware of incidents. However, a 450 MHz passive radar—standalone or as part of a heterogeneous sensor system—will enable drone detection and tracking and thus open the possibility for countermeasures.

In addition, the special requirements for close range monitoring of energy infrastructures must be taken into account: Above all, intrusion detection systems must not interfere with the critical communicative connection of energy infrastructures, which in future will primarily take place via the fail-safe 450 MHz radio network currently being rolled out.

Against this background, we proved in experiments with single and multi-channel passive radar systems that the 450 MHz radio network is a suitable illumination infrastructure for a passive radar solution. The 450 MHz radio network offers an inherent advantage regarding availability, robustness and planning reliability. The 450 MHz radio network is designed to be blackout-proof and, in the event of an emergency, to enable voice communication for 72 h. This means that continued operation of the passive radar can also be guaranteed in the event of a crisis or disaster. In addition, the 450 MHz radio network will remain in use for the energy industry for many years to come, outliving many current passive radar illuminators as a reliable illumination infrastructure.

Future work could focus on analysis of the detection range for different types of drones. Additionally, the comparison and fusion with other passive radar illuminators (DVB-T, commercial mobile communications) as well as with heterogeneous sensors (radio direction finders, cameras, acoustic systems, active radar) is of great interest.

Author Contributions

Both Bruno Demissie and Christian Steffes took part in the conceptualization, data evaluation, analysis and visualization and writing of the original draft. Bruno Demissie developed the theory and methodology for signal processing. Christian Steffes took part in performing the experiments and took care of funding acquisition and project administration.

Acknowledgements

The authors thank Matthias Mandt for his work on our experimental systems, for preparing and conducting the measurement campaigns and for his expertise in evaluating the experiments. Without him, the results would not have been possible. This research was partially supported by BDEW Bundesverband der Energie- und Wasserwirtschaft e.V. and 450connect GmbH. We thank Mathias Böswetter from BDEW for his contributions regarding the concept and use cases. We thank Dr. Andrzej Cwik and Dr. Frederik Giessing from 450connect GmbH while providing real LTE450 downlink signals for their support and expertise. Open Access funding enabled and organized by Projekt DEAL.

Funding

This research was partially funded by the German Federal Ministry of Defence, the BDEW Bundesverband der Energie- und Wasserwirtschaft e.V. and 450connect GmbH.

Conflicts of Interest

The authors declare no conflicts of interest.

Data Availability Statement

The authors have nothing to report.

References

1. P. E. Howland, "Special Issue on Passive Radar Systems," *IET Radar, Sonar & Navigation* 152, no. 3 (2005).

2. P. Howland, H. Griffiths, and C. Baker, "Passive Bistatic Radar Systems," in *Bistatic Radar: Emerging Technology*, ed. M. E. Cherniakov (John Wiley and Sons, 2008), 247–313.

3. H. Kuschel, "Approaching 80 Years of Passive Radar," in *IEEE* (International Conference on Radar, 2013), 213–217.

4. H. S. Sun, D. K. P. Tan, L. Yilong, and M. Lesturgie, "Applications of Passive Surveillance Radar System Using Cell Phone Base Station Illuminators," *IEEE Aerospace and Electronic Systems Magazine* 25, no. 3 (2010): 10–18, https://doi.org/10.1109/maes.2010.5463951.

5. H. Griffiths, A. Garnett, C. Baker, and S. Keaveney, "Bistatic Radar Using Satellite-Borne Illuminators of Opportunity," in *IEEE*, Vol. 92 (Proceedings of International Conference Radar, 1992), 276–279.

6. F. Colone, K. Woodbridge, H. Guo, D. Mason, and C. J. Baker, "Ambiguity Function Analysis of Wireless LAN Transmissions for Passive Radar," *IEEE Transactions on Aerospace and Electronic Systems* 47, no. 1 (2011): 240–264, https://doi.org/10.1109/taes.2011.5705673.

7. K. Chetty, G. Smith, and K. Woodbridge, "Through-The-Wall Sensing of Personnel Using Passive Bistatic Wifi Radar at Standoff Distances," *IEEE Transactions on Geoscience and Remote Sensing* 50, no. 4 (2012): 1218–1226, https://doi.org/10.1109/tgrs.2011.2164411.

8. D. Poullin, "Uav Detection and Localization Using Passive DVB-T Radar MFN and SFN," *NATO, MP-SET-231-18* (2016): 1–9.

9. L. Yuqi, W. Xianrong, T. Hui, Y. Jianxin, C. Yiyao, and Z. Xun, "Digital Television Based Passive Bistatic Radar System for Drone Detection," in *IEEE Radar Conference (RadarConf)* (IEEE, 2017): 1493–1497.

10. E. Vorobev, V. Veremyev, and N. Tulenkov, "Experimental DVB-T2 Passive Radar Signatures of Small UAVs," in *2019 Signal Processing Symposium (SPSympo)* (IEEE, 2019), 67–70.

11. T. Martelli, F. Colone, and R. Cardinali, "DVB-T Based Passive Radar for Simultaneous Counter-Drone Operations and Civil Air Traffic Surveillance," *IET Radar, Sonar & Navigation* 14, no. 4 (2020): 505–515, https://doi.org/10.1049/iet-rsn.2019.0309.

12. S. Rzewuski, K. Kulpa, M. Pachwicewicz, M. Malanowski, and B. Salski, "Drone Detectability Feasibility Study Using Passive Radars Operating in WIFI and DVB-T Band," *NATO-MP-MSG-SET* 183 (2021): 1–13, http://publications.sto.nato.int/publications/STO%20meeting%20Proceedings/STO-MP-MSG-SET-183/MP-MSG-SET-183-13.pdf.

13. M. P. Malanowski, G. K, M. Zywek, M. Szczepankiewicz, and P. Samczynski, "Drone Detection Experiment Using DVB-T-based Passive Radar," in *Proceedings of 6th PCL Focus Days* (Fraunhofer FHR, 2017).

14. C. Schüpbach, C. Patry, F. Maasdorp, U. Böniger, and P. Wellig, "Micro-UAV Detection Using DAB-based Passive Radar," in *IEEE Radar Conference* (IEEE, 2017), 1037–1040.

15. S. Welschen, C. Schüpbach, S. Paine, U. Böniger, P. Leuchtmann, and J. Leuthold, "Localization of Micro Unmanned Aerial Vehicles Using Digital Audio Broadcast Signals," in *IEEE Radar Conference* (IEEE, 2020), 1–6.

16. C. Steffes, B. Demissie, B. Knödler, M. Brötje, M. Mandt, and W. Koch, "Passive Radar Using Mobile Communication: A Discussion of Use Cases and Feasibility," in *IEEE Radar Conference* (IEEE, 2022).

17. C. Steffes, B. Demissie, M. Mandt, and M. Böswetter, "Surveillance of Critical Infrastructure Using the lte450 Network as Passive Radar Illuminator: Feasibility Study and Range Assessment," in *Sensor Data Fusion: Trends, Solutions, Applications (SDF)* (IEEE, 2022).

18. T. Kürner, "Propagation Models for macro-cells," in *European Commission, COST 231: Evolution of Land Mobile Radio (Including Personal) Communications*, (1997).

19. B. R. Mahafza, *Radar Systems Analysis and Design Using MATLAB, Third Edition* (CRC Press, Taylor and Francis Group, 2013).

20. M. Demissie, B. Böswetter, M. Mandt, and C. Steffes, "Protection of Critical Infrastructure Using LTE450-based Passive Radar: Range Measurements for Drone Detection," in *IEEE, Rennes, France, International Radar Conference (RADAR)*, (2024).

21. ETSI (2020), "LTE; Evolved Universal Terrestrial Radio Access (E-UTRA); Physical Channels and Modulation," version 16.3.0: 3GPP TS 36.211, www.etsi.org.

22. C. R. Berger, B. Demissie, J. Heckenbach, P. Willett, and S. Zhou, "Signal Processing for Passive Radar Using OFDM Waveforms," *IEEE Journal of Selected Topics in Signal processing* 4, no. 1 (2010): 226–238, https://doi.org/10.1109/jstsp.2009.2038977.

23. B. Demissie, "Verfahren und Vorrichtung zum Bestimmen einer Zeitverzögerung und einer Frequenzverschiebung zwischen einem an einem bewegten Objekt gestreuten Funksignal und dem ungestreuten Funksignal oder einem in bekannter Weise gestreuten Funksignal in einem Mehrwegesignal," *Deutsches Patent und Markenamt* (2011): DE 20 2011 017 734.5.

24. M. H. Ackroyd and F. Ghani, "Optimum Mismatched Filters for Sidelobe Suppression," *IEEE Transactions on Aerospace and Electronic Systems* 9, no. 2 (1973): 214–218, https://doi.org/10.1109/taes.1973.309769.

25. J. L. Garry, C. J. Baker, and G. E. Smith, "Evaluation of Direct Signal Suppression for Passive Radar," *IEEE Transactions on Geoscience and Remote Sensing* 55, no. 7 (2017): 3786–3799, https://doi.org/10.1109/tgrs.2017.2680321.

26. B. Demissie, "Clutter Cancellation in Passive Radar Using GSM Broadcast Channels," *IET Radar, Sonar & Navigation* 8, no. 7 (2013): 787–796, https://doi.org/10.1049/iet-rsn.2013.0042.

27. N. D. Sidiropoulos, R. Bro, and G. B. Giannakis, "Parallel Factor Analysis in Sensor Array Processing," *IEEE Transactions on Signal Processing* 48, no. 8 (2000): 2377–2388, https://doi.org/10.1109/78.852018.